

1 Precovery Observations of 3I/ATLAS from TESS Suggests Possible Distant Activity

2 ADINA D. FEINSTEIN  ^{1,*} JOHN W. NOONAN  ² AND DARRYL Z. SELIGMAN  ^{1,†}

3 ¹*Department of Physics and Astronomy, Michigan State University, East Lansing, MI 48824, USA*

4 ²*Department of Physics, Auburn University, Edmund C. Leach Science Center, Auburn, 36849, AL, USA*

ABSTRACT

5 3I/ATLAS is the third macroscopic interstellar object detected traversing the Solar System. Since
6 its initial discovery on UT 01 July 2025, hundreds of hours on a range of observational facilities have
7 been dedicated to measure the physical properties of this object. These observations have provided
8 astrometry to refine the orbital solution, photometry to measure the color, a rotation period and secular
9 light curve, and spectroscopy to characterize the composition of the coma. Here, we report precovery
10 photometry of 3I/ATLAS as observed with NASA's *Transiting Exoplanet Survey Satellite* (*TESS*).
11 3I/ATLAS was observed nearly continuously by *TESS* from UT 07 May 2025 to 02 June 2025. We
12 use the shift-stack method to create deep stack images to recover the object. These composite images
13 reveal that 3I/ATLAS has an average *TESS magnitude* of $T_{\text{mag}} = 20.83 \pm 0.05, 19.28 \pm 0.05$ and
14 an absolute visual magnitude of $H_V = 13.72 \pm 0.35; 12.52 \pm 0.35$, the latter being consistent with
15 magnitudes reported in July 2025. When coupled with recent HST images deriving a nucleus
16 size of $R < 2.8$ km ($H > 15.4$), our measurements suggest that 3I/ATLAS may have been active
17 out at ~ 6 au. Additionally, we extract a ~ 20 day light curve and find no statistically significant
18 evidence of a nucleus rotation period. Nevertheless, the data presented here are some of the earliest
19 precovery images of 3I/ATLAS and may be used in conjunction with future observations to constrain
20 the properties of our third interstellar interloper.

21 **Keywords:** Asteroids (72) — Comets (280) — Interstellar Objects (52) — Photometry (1234)

1. INTRODUCTION

22 Interstellar objects (ISOs) offer unique insights into
23 the formation conditions of rocks and ices in regions of
24 our galaxy beyond the Solar System. The recent discov-
25 ery of the third ISO, 3I/ATLAS, was reported on UT 01
26 July 2025 (L. Denneau et al. 2025) by the ATLAS survey
27 (J. L. Tonry et al. 2018a,b). This discovery increases
28 the current census of discovered macroscopic ISOs by
29 50%. Since its discovery, there has been an international
30 rush to observe 3I/ATLAS before it is no longer visi-
31 ble to observers in February 2026. In particular, early
32 telegrams reported activity in images from the Nordic-
33 Optical Telescope (D. Jewitt & J. Luu 2025) and the
34 Two-meter Twin Telescope (M. R. Alarcon et al. 2025).
35 Preliminary reconnaissance observations revealed a red-
36 dened reflectance spectrum similar to D-type asteroids,
37 no clear photometric variability and faint cometary ac-

39 tivity (T. Karetta et al. 2025; R. de la Fuente Marcos
40 et al. 2025; C. Opitom et al. 2025; D. Z. Seligman et al.
41 2025; B. Yang et al. 2025).

42 Two macroscopic scale ISOs had been discovered be-
43 fore 3I/ATLAS: 1I/‘Oumuamua in 2017 (G. V. Williams
44 et al. 2017) and 2I/Borisov in 2019 (G. Borisov et al.
45 2019). The light curve of 1I/‘Oumuamua was markedly
46 different from the 3I/ATLAS because it exhibited dras-
47 tic brightness variations (M. Drabus et al. 2017; W. C.
48 Fraser et al. 2018; M. M. Knight et al. 2017; M. J. S.
49 Belton et al. 2018). This was presumably due to
50 an elongated 6 : 6 : 1 oblate spheroid geometry (S.
51 Mashchenko 2019; A. G. Taylor et al. 2023) and a lack
52 of cometary activity (D. Jewitt et al. 2017; K. J. Meech
53 et al. 2017; Q.-Z. Ye et al. 2017). A significant non-
54 detection of 1I/‘Oumuamua with the *Spitzer* space tele-
55 scope provided upper limits on the production of carbon-
56 based species (D. E. Trilling et al. 2018). However,
57 1I/‘Oumuamua had significant radial nongravitational
58 acceleration in its trajectory (M. Micheli et al. 2018).
59 1I/‘Oumuamua had a reddened color like 3I/ATLAS
60 (M. T. Bannister et al. 2017; A. Fitzsimmons et al.

Email: adina@msu.edu

* NASA Sagan Fellow

† NSF Astronomy and Astrophysics Postdoctoral Fellow

61 2018; J. Masiero 2017) and a low velocity at infinity
 62 indicating a young kinematic age (E. Gaidos et al. 2017;
 63 E. Mamajek 2017). On the contrary, 2I/Borisov
 64 displayed distinct cometary activity (D. Jewitt & J. Luu
 65 2019; A. Fitzsimmons et al. 2019; T. Karetta et al. 2020;
 66 C. Opitom et al. 2019; M. T. Bannister et al. 2020; D.
 67 Bodewits et al. 2020; G. Cremonese et al. 2020; M. A.
 68 Cordner et al. 2020; P. Guzik et al. 2020; M.-T. Hui
 69 et al. 2020; Y. Kim et al. 2020; H. W. Lin et al. 2020;
 70 A. J. McKay et al. 2020; Z. Xing et al. 2020; K. Aravind
 71 et al. 2021; S. Bagnulo et al. 2021; B. Yang et al. 2021;
 72 S. E. Deam et al. 2025). For reviews on ISOs discovered
 73 passing through the solar system prior to 3I/ATLAS,
 74 we refer the reader to A. Moro-Martín (2022); D. Jewitt
 75 & D. Z. Seligman (2023); D. Z. Seligman & A. Moro-
 76 Martín (2023); A. Fitzsimmons et al. (2024).

77 Precovery observations of small bodies such as comets,
 78 asteroids, and ISOs can provide constraints on critical
 79 physical properties such as orbit, size, composition, and
 80 activity. For example, M.-T. Hui & M. M. Knight (2019)
 81 searched for precovery detections of 1I/‘Oumuamua in
 82 Solar and Heliospheric Observatory (SOHO) and Solar
 83 TERrestrial RElations Observatory (STEREO) images.
 84 Their search provided nondetections, but these nonde-
 85 tections provided critical upper limits on the produc-
 86 tion rate of dust and water at low heliocentric distances
 87 — during a regime of 1I/‘Oumuamua’s trajectory which
 88 was entirely unconstrained from extant observations. Q.
 89 Ye et al. (2020) reported pre-discovery observations of
 90 2I/Borisov in survey data from the Zwicky Transient
 91 Facility (ZTF), as well as a comprehensive search of
 92 Catalina Sky Survey and Pan-STARRS data for the
 93 object. The combination of precovery detections and non-
 94 detections provided valuable upper limits on the size of
 95 the nucleus and information regarding the volatility of
 96 ices driving activity. Thus far for 3I/ATLAS, D. Z. Selig-
 97 man et al. (2025) reported ZTF observations dating back
 98 to UT 2025 May 22 and C. O. Chandler et al. (2025) re-
 99 ported observations of using the NSF-DOE Vera C. Ru-
 100 bin Observatory Science Verification (SC) images dating
 101 back to UT 2025 June 21. The Rubin Observatory SC
 102 observations also revealed faint activity.

103 All four aforementioned studies highlight the
 104 strengths of all-sky surveys in searching for precovery
 105 observations. Although not its original science purpose,
 106 NASA’s *Transiting Exoplanet Survey Satellite* (*TESS*;
 107 G. R. Ricker et al. 2015) has also been able to recover
 108 and discover small bodies in the solar system (A. Pál
 109 et al. 2020; G. M. Szabó et al. 2022; C. Kiss et al. 2025)
 110 as well as characterize cometary activity (T. L. Farnham
 111 et al. 2019, 2021). *TESS* has a large on-sky coverage
 112 due to the orientation of four wide-field cameras, where

113 each camera has a field-of-view of $24^\circ \times 24^\circ$, amounting
 114 to a total FOV of $96^\circ \times 24^\circ$. These images, known as
 115 the *TESS* Full-Frame Images (FFIs), are made avail-
 116 able to the community. *TESS* observes a single field for
 117 ~ 27 days, providing a long photometric baseline for
 118 variability studies. While limited in its resolution for
 119 morphology analysis of cometary comae due to its large
 120 pixel scale, *TESS* is excellent for long-term photometric
 121 monitoring and analysis.

122 During the primary mission, *TESS* exclusively ob-
 123 served the northern and southern ecliptic hemispheres.
 124 However, in its extended missions, *TESS* was reoriented
 125 to observe the ecliptic plane for 10 nonconsecutive sec-
 126 tors. One of these sectors — both fortuitously and
 127 serendipitously — happened to observe the exact region
 128 where 3I/ATLAS was located. Here, we report the pre-
 129 recovery detection of 3I/ATLAS in the *TESS* Full-Frame
 130 Images (FFIs). This manuscript is organized as follows.
 131 In Section 2, we present the *TESS* observations and dis-
 132 cuss our processing of the FFIs. We present the results
 133 of our search in Section 3. We conclude in Section 4.
 134 The  icon affiliated with all figures links to the Python
 135 script and data used to generate that figure.

2. TESS OBSERVATIONS

136 *TESS* re-observed part of the ecliptic plane during
 137 Cycle 7 of its second extended mission. Upon discovery
 138 of 3I/ATLAS, we used `tess-point` (C. J. Burke et al.
 139 2020) in conjunction with 3I/ATLAS’ best-fit orbital sol-
 140 ution from the JPL Horizons Small Bodies Database³
 141 to determine if the object was in the *TESS* FOV. We
 142 found that 3I/ATLAS was observed during Sector 92,
 143 which occurred from UT 07 May through 03 June 2025.

144 Each of *TESS*’s four cameras are divided into four
 145 charged-coupled devices (CCDs). Due to its high ve-
 146 locity, 3I/ATLAS was observed on two Camera-CCD
 147 pairings throughout the sector: Camera 2 CCD 3 and
 148 Camera 1 CCD 2. These are located next to each other
 149 in the orientation presented in Figure 1. Each *TESS*
 150 FFI has an exposure time of 200 seconds. The data is
 151 downloaded every ~ 7 days from the spacecraft due to
 152 the increased data volume of the higher cadence FFIs.
 153 These downlink times occur near apogee and perigee of
 154 the orbit of the spacecraft and thereby result in short
 155 gaps in the data. The total duration of science data
 156 collected during Sector 92 is 26.05 days.

2.1. FFI Selection and Background Removal

158 We downloaded all **calibrated** FFIs for Camera 2
 159 CCD 3 and Camera 1 CCD 2 using the bulk down-
 160

³ <https://ssd.jpl.nasa.gov/>

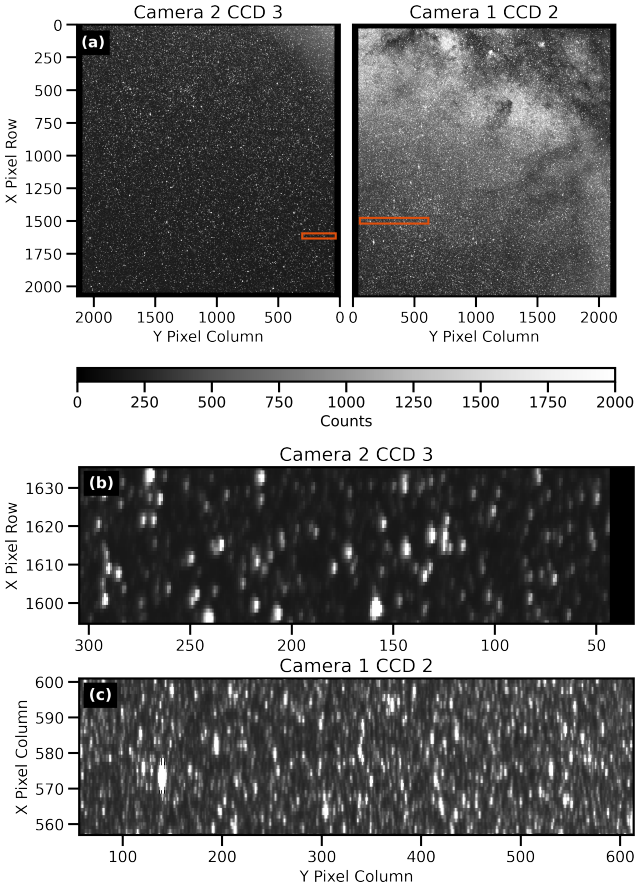


Figure 1. The calibrated *TESS* FFIs. (a) An example exposure of a full FFI for Camera 2 CCD 3, left, and Camera 1 CCD 2, right. We highlight the region where 3I/ATLAS was observed on both detectors by the orange box. (b) A zoom-in of the field in Camera 2 CCD 3. We note that columns 0 – 44 are serial register columns and are not used in our analysis. (c) A zoom-in of the field in Camera 1 CCD 2. 3I/ATLAS enters a much more crowded field, closer to the ecliptic plane, throughout the sector. All images share the same color scaling. 

load scripts provided by the Mikulski Archive for Space Telescopes (MAST)⁴. 3I/ATLAS was observed on pixels $x = [1592, 1635]$; $y = [0, 305]$ on Camera 2 CCD 3 and pixels $x = [556, 601]$; $y = [39, 614]$ on Camera 1 CCD 2. We highlight example images of these two regions in Figure 1. It is important to note that columns 0 – 44 are serial register columns, columns 2092 – 2136 are virtual columns, and rows 2048 – 2078 are buffer, smear, and virtual rows; none of these regions can be used for science.

The *TESS* FFIs are contaminated by both zodiacal light and scattered earthshine contamination. In

particular, the scattered earthshine manifests as strong ramps at the beginning and end of each *TESS* orbit (~ 13 days). While the background typically varies smoothly, there have been instances of more sporadic and variable behavior (Figure 2). To identify highly contaminated FFIs, we calculated the median value in each FFI. The FFIs containing highly non-smooth variability, as identified by-eye, are entirely removed from our analysis (Figure 2). This resulted in the removal of 9% of the available FFIs from Camera 2 CCD and 5% of the available FFIs from Camera 1 CCD 2. In total, after these data-quality cuts, we analyzed 9837 FFIs (353 GB). We provide more specific details pertaining to each Camera/CCD configuration in Table 1.

We fit and subtract the background from all remaining FFIs after the heavily contaminated ones were removed. Working with the entire FFI is unnecessary. Instead, we create a “postcard” cutout (A. D. Feinstein et al. 2019) of the entire region where 3I/ATLAS is visible in the FFI (orange boxes in the upper two panels and full bottom two panels in Figure 1). Previous search and recovery analyses of known solar system bodies with *TESS* have fit pixel variability using an n^{th} -order polynomial (e.g. C. Kiss et al. 2025). We experimented with two methods to remove background contamination from these observations. First, we fit a 2nd-order polynomial to the background, similar to C. Kiss et al. (2025). We fit each continuous section of the light curve with these models, i.e. we chunk the observations based on gaps in the *TESS* data. This leaves a total of five different segments that are fit (two segments for Camera 2 CCD 3; three segments for Camera 1 CCD 2). This experiment demonstrated that a 2nd-order polynomial fits the baseline well, but fails to fit the orbital ramps (Figure 10).

Second, we fit the background with a data-driven Savitsky-Golay filter with a pre-defined window length and a 2nd-order polynomial. We repeat the same process of chunking the light curve based on gaps in the observations. We test several window lengths ranging from 31 – 901 pixels. The residuals of several example model fits are presented in Figure 10. This experiment revealed that smaller window sizes removed astrophysical signals, while larger windows did not capture the variability of the orbital ramps. Therefore, we settled on using an average window length of 307 pixels.

⁴ <https://archive.stsci.edu/missions-and-data/tess>

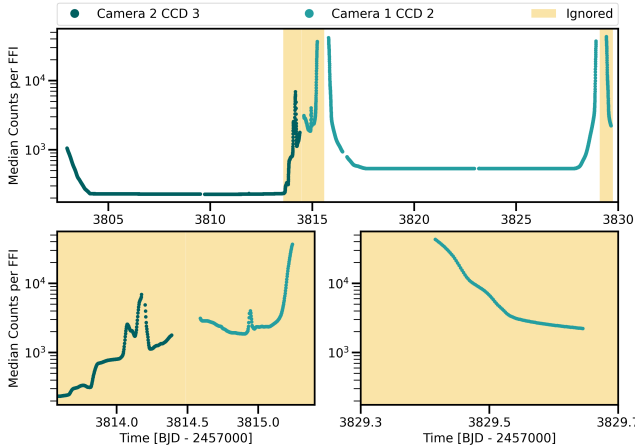


Figure 2. The calibrated median counts per FFI when 3I/ATLAS is within the FOV. We highlight the strong orbital ramps, gaps, and systematics which were present in Sector 92. We choose to remove FFIs which demonstrated sharp variability and/or had unexpected gaps. These frames were visually identified and are highlighted in the bottom two subplots. FFIs not used in this analysis are highlighted in yellow. ♀

Table 1. The locations of 3I/ATLAS and corresponding *TESS* Camera/CCD times and pixel locations throughout Sector 92. We denote the number of analyzed FFIs, N_{FFIs} , per Camera/CCD. We note that the *TESS* BJD [TBJD] time is given in units of BJD - 2457000. We denote the heliocentric and geocentric distances as d_{\odot} and d_{TESS} , respectively. We denote our derived *TESS* magnitude, T_{mag} , visual magnitude, V , and absolute visual magnitude, H_V .

Camera/ CCD	2/3	1/2
Start [TBJD]	3802.975926	3815.799580
End [TBJD]	3813.474497	3828.911416
Start [UTC]	2025-05-07 11:24:43	2025-05-20 07:10:47
End [UTC]	2025-05-17 23:22:39	2025-06-02 09:51:49
x pixel range	[1592, 1635]	[556, 601]
y pixel range	[0, 305]	[39, 614]
d_{\odot} [au]	6.35 - 5.99	5.92 - 5.47
d_{TESS} [au]	6.36 - 6.02	5.92 - 5.48
N_{FFI}	4399	5438
T_{mag}	20.83 ± 0.05	19.28 ± 0.05
V	21.63 ± 0.35	20.08 ± 0.35
H_V	13.72 ± 0.35	12.52 ± 0.35

2.2. Removing Crowded Frames

Due to the crowdedness in some of the images, we create a filter to remove images which

may have significant stellar contamination. The final deepstack images in this work only include frames that are not significantly contaminated. The contamination criteria is defined as the following: Because we are only interested in crowding near the location of 3I/ATLAS, we only consider sources within an 11×11 window around the central location. We use `astropy.stats.sigma_clip` to determine how many pixels are $> 2\sigma$ outliers compared to the mean value. We assume the default settings for `astropy.stats.sigma_clip`, other than defining the σ value. We mask any frame for which more than half of the pixels within this region are flagged as $> 2\sigma$ outliers. Examples of non-crowded versus crowded frames are shown in Figure 3.

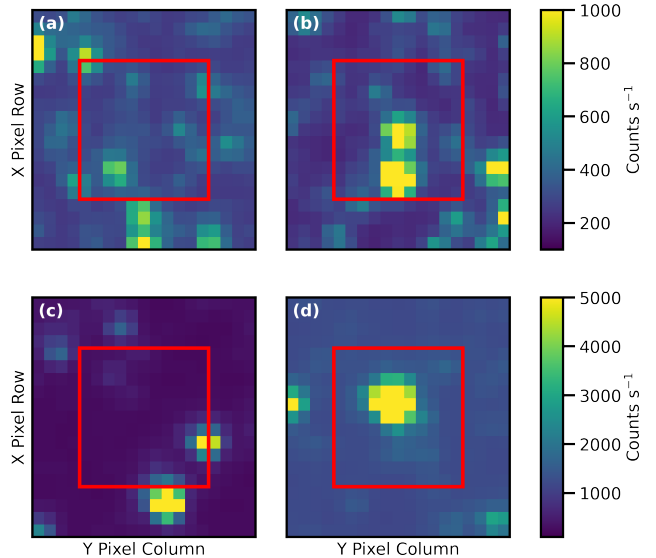


Figure 3. Examples of calibrated FFI cutouts that are included (a/c) and excluded (b/d) from our deepstack image. The first and second row contains images from Camera 2 CCD 3 and Camera 1 CCD 2 respectively. The red box highlights the region we search to remove outlier images. We take this interior cutout and run it through `astropy.stats.sigma_clip` using $\sigma = 2$. We mark images as bad when over half of the pixels within this box are $> 2\sigma$ above the average value. This sufficiently removes images where the path of 3I/ATLAS crosses background sources. ♀

2.3. Deep Image Creation

After the background models are removed, we employ a shift-stack algorithm to create a *TESS* deepstack image. We choose not to combine images across detectors,

as they may have different systematics. Our algorithm works as follows: (I) Query the location of 3I/ATLAS from the JPL Horizons Small Bodies Database for each FFI; (II) Use the world coordinate system information to convert the queried (RA, Dec) to the (x,y) pixel location of 3I/ATLAS. We convert the (x, y) location from float values to integers using `np.round`, in order to accurately determine the nearest pixel; (III) Create a 17×17 pixel cutout centered on the integer (x, y) coordinates where 3I/ATLAS is expected to be; (IV) Repeat this procedure for all integrations; (V) Sum all of the images. Additionally, due to the apparent location with respect to the galactic plane, we create a data quality flag to track particularly crowded fields. The shift-stack technique implemented in this paper works well for objects with known orbital parameters, but may be more computationally inefficient when completing a blind-search for new objects. However, it has been employed with some success for example by W. C. Fraser et al. (2024) — albeit using more sensitive data. A coarse summation presented here is sufficient for *TESS* due to its large pixel scale.

2.4. Recovery of Known Minor Planet 896 Sphinx

We validated our algorithm by recovering another small body which was observed in the same field as 3I/ATLAS. We find that the known main-belt minor planet 896 Sphinx (A918 PE) ($H_V \approx 15$) was observed on Camera 2 CCD 3. 896 Sphinx was initially discovered in 1918 by M. Wolf. It has a known diameter of 11.9 km (J. R. Masiero et al. 2014) and rotation period of 21.038 ± 0.008 hours (T. Polakis 2018). We apply our background-correction and shift-stack method outlined above to the region where 896 Sphinx is within the FFIs.

We present the deepstack image of 896 Sphinx in Figure 4. We find that we are able to recover 896 Sphinx at 6.6σ . Additionally, we extract a light curve using a 3×3 -pixel mask centered on 896 Sphinx. We present the extracted normalized light curve and associated errors in Figure 4. We run this light curve through a Lomb-Scargle periodogram (N. R. Lomb 1976; J. D. Scargle 1982) to recover the known rotation period of the object. We find that periods $P < 10$ hours are dominated by instrumental noise. We ignore these periods. We find the peak of max power for $P > 10$ hours. We fit this peak with a Gaussian function and optimize our fit using a non-linear least squares approach. We find that the peak occurs at 21.858 ± 0.577 hours. Our error is adopted from the width of the best-fit Gaussian. Our recovered period is within 1.5σ of the period presented in T. Polakis (2018). The

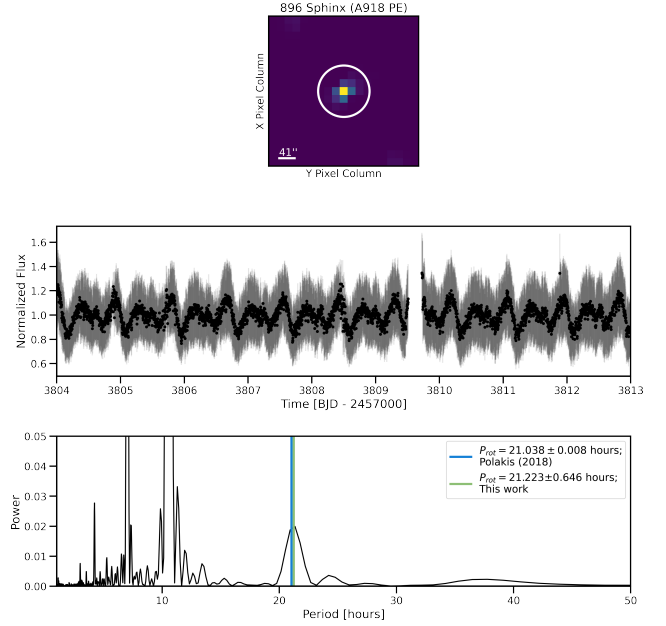


Figure 4. Deepstacked image (top left), light curve with errors (top right), and periodogram (bottom right) of the main belt minor planet 896 Sphinx. 896 Sphinx is highlighted in the image by a white circle. We provide the *TESS* pixel scale in the bottom left. We use this object, with an apparent $H = 15$ as a demonstration of our implemented technique to recover 3I/ATLAS. 896 Sphinx has a measured rotation period of 21.038 ± 0.008 hours (T. Polakis 2018). We find the best-fit period of this object from *TESS* is 21.858 ± 0.577 hours, which is within 1.5σ agreement with T. Polakis (2018). The discrepancy between periods is likely due to the lack of *TESS* sensitivity of faint objects. These images were stacked from Camera 2 CCD 3. \bullet

discrepancy between our rotation period and the archival rotation period may be due to the lack of sensitivity of *TESS* for faint objects.

2.5. Recovery of 3I/ATLAS

Figure 5 shows the background-removed deepstack images and associated errors of 3I/ATLAS as observed by *TESS*. These deepstacks are limited to cutouts which are not overcrowded with bright sources, as defined in Section 2.2. The median, mean, and summed images are shown for both detectors. The detection threshold for 3I/ATLAS is calculated by propagating errors from the calibrated FFIs. Although the median deepstack images are implemented for the remainder of this paper, it should be noted that 3I/ATLAS is visible by-eye in all three types of images in Figure 5. The central pixel in Camera 2 CCD 3 has a median counts value of 0.173 ± 0.004

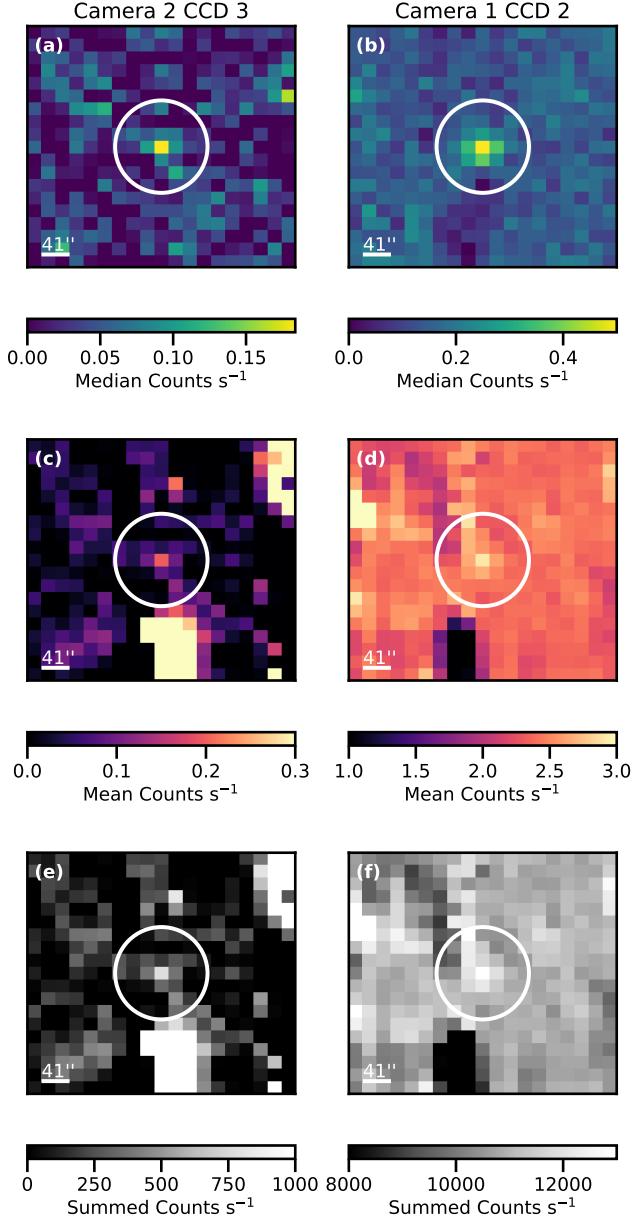


Figure 5. Deepstacked background-removed images of 3I/ATLAS in the *TESS* FFIs. We present two images per Camera/CCD pairing, labeled at the top of the columns. Panels a/b, c/d, and e/f are the median, mean, and summed stacked images, respectively. 3I/ATLAS is centered in each image and is highlighted with a white circle. We limited the stacked FFIs to cutouts which are not overcrowded with bright sources, as defined in Section 2.2. Due to the large pixel scale of *TESS* (bottom left), we are unable to resolve any astrometric information from the images. \bullet

$e^- s^{-1}$. The background scatter is calculated as the median and standard deviation of the singular pixels surrounding the central pixel exercise.

The background has an averaged count value of $0.022 \pm 0.008 e^- s^{-1}$. Therefore, we are able to recover 3I/ATLAS at 19σ in this summed deepstack image. The same exercise is repeated for Camera 1 CCD 2. The central pixel in this image has a summed counts value of $0.589 \pm 0.016 e^- s^{-1}$. The background has an averaged count value of $0.141 \pm 0.039 e^- s^{-1}$. Therefore, we are able to recover 3I/ATLAS at 11σ in this summed deepstack image. It is not surprising that we are unable to recover 3I/ATLAS at the same high fidelity as the previous image. This is because the field becomes increasingly more crowded as 3I/ATLAS' apparent motion places it closer to the galactic plane.

3. RESULTS

3I/ATLAS has displayed visible cometary activity months prior to perihelion. It is feasible that the level of activity has changed and will continue to change throughout its orbit. Light curves from images when 3I/ATLAS was at further heliocentric distances could provide insights into variations in the activity and nucleus properties such as the rotation period. In this section, we therefore extract the 20-day *TESS* light curve and calculate the resulting secular light curve of 3I/ATLAS.

3.1. Magnitude Calculation

We use a 3×3 pixel aperture on the median deepstacked image to calculate the magnitude of 3I/ATLAS. We convert the calibrated flux in $e^- s^{-1}$ to *TESS* magnitude using the following relationship:

$$T_{\text{mag}} = -2.5 \log_{10}(c) + 20.44. \quad (1)$$

In Equation 1, c is the number of counts per second. This conversion is provided in the *TESS* Instrumental Handbook (R. Vanderspek et al. 2018). We adopt the error on the zeropoint of 0.05 mag. We note that while the zeropoint may change slightly between sectors, cameras, and/or CCDs, it is standard practice to not recalculate the value for each observation combination (e.g. T. L. Farnham et al. 2019; M. M. Fausnaugh et al. 2023; J. E. Andrews et al. 2025). We calculate T_{mag} using a 3×3 aperture on the median deepstack images presented in Figure 5. For Camera 2 CCD 3, we derive $c_{23} = 0.699 \pm 0.004 e^- s^{-1}$. For Camera 1 CCD 2, we derive $c_{12} = 2.904 \pm 0.016 e^- s^{-1}$.

We find that 3I/ATLAS has a $T_{\text{mag}} = 20.83 \pm 0.05$ in the Camera 2 CCD 3 image and a $T_{\text{mag}} = 19.28 \pm 0.05$ in the Camera 1 CCD 2 image.

Our calculated T_{mag} is in agreement with [J. Martinez-Palomera et al. \(2025\)](#). Examining the origins of slight offsets between our extracted values is beyond the scope of this work. These two magnitudes are averaged over the two observing windows in Table 1, which span a range in heliocentric distance of 6.4 to 5.4 au, respectively. In that same time period the distance between 3I/ATLAS and the TESS spacecraft decreased by 0.9 au. The rapid change in both these properties can be used to constrain any changes to the overall activity of 3I/ATLAS between both times.

From geometric effects alone, and ignoring the small ($\sim 2.5^\circ$) phase angle change, we would expect the flux from 3I to increase by a factor of 1.5. Converting this back into magnitudes we expected 3I/ATLAS to have a measured magnitude of **20.5** in the Camera 1 CCD 2 images, rather than the observed T_{mag} of **19.28**, indicating a factor of 5 increase in the flux, rather than 1.5. Within our uncertainty on the TESS magnitude, our observations are statistically inconsistent with an asteroid-like reflectance model that ignores dust production.

3.2. Photometric Light Curve

We extract a light curve using the same 3×3 -pixel aperture and propagate the errors from the calibrated FFIs. We normalize the light curve. Additionally, we bin our light curve to 36-minute bins. We analyze the binned light curve with a Lomb-Scargle periodogram to search for evidence of periodicity. We do this for each light curve independently. We search for a rotation period between $P_{\text{rot}} = 1 - 70$ hours, which is mostly consistent with P_{rot} of other kilometer scale small bodies in the solar system ([B. D. Warner et al. 2009](#)). Both of the light curves and affiliated periodograms are presented in Figure 6.

There are several similarities between the Lomb-Scargle periodograms. First, we find that $P_{\text{rot}} < 10$ hours are dominated by noise and/or unremoved systematics. Second, we see that there is no agreement between periodograms at $P > 40$ hours. Third, we see a some strong periodicity between 10-30 hours. This is more apparent in the light curve from Camera 1 CCD 2, when 3I/ATLAS 0.4 au closer. In particular, we find a peak in the periodogram close to the recently recovered period of 16.16–16.79 hours presented in [R. de la Fuente Marcos et al. \(2025\)](#); [T. Santana-Ros et al. \(2025\)](#).

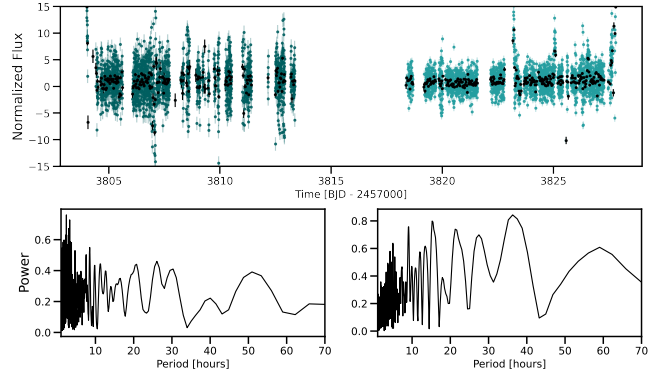


Figure 6. Compiled normalized TESS light curve of 3I/ATLAS and associated error bars. We bin the light curve to ~ 36 minutes in black. These TESS data offer an advantage when trying to measure the nucleus' rotation period, as 3I/ATLAS was farther from perihelion. We run the binned light curve through a Lomb-Scargle periodogram (bottom panels). We do not find similarities in periods between both light curves. \bullet

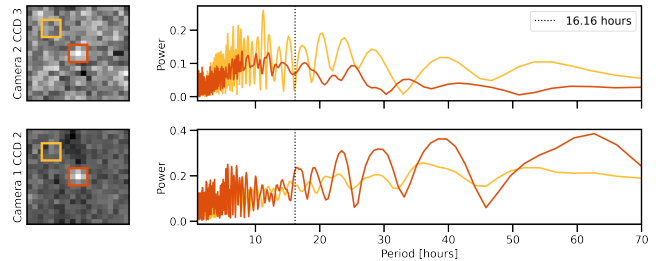


Figure 7. Comparison of the Lomb-Scargle periodogram for 3I/ATLAS (orange) and a background pixels (yellow). We select a pixel in the same location across both images. We mark the recently hypothesized rotation period of 3I/ATLAS as a horizontal dotted line ([R. de la Fuente Marcos et al. 2025](#); [T. Santana-Ros et al. 2025](#)). The background pixels here are representative of systematics seen across all pixels within a 5×5 region around the central pixel. We find that the light curve and resulting periodogram are dominated by noise and therefore we cannot constrain the rotation period of the nucleus. \bullet

To further assess this potential rotational signature, we run the same Lomb-Scargle test for a nearby background pixels in the FFI. Because the background can rapidly vary across the TESS detector, we select an example background pixel within 5-pixels of 3I/ATLAS. The results of this test are presented in Figure 7. We find that the background pixel periodogram for Camera 2 CCD 3 shows a similar peak at ~ 16 hours, but we do not see a similarly strong peak around this time for Camera 1 CCD 2. However, there are stronger periodic peaks in this periodogram, so it is challenging to assess

whether or not this 16 hour period is physically motivated by the *TESS* observations alone.

We complete this exercise for all of the pixels within a 5×5 region around 3I/ATLAS. We pay particular attention to pixels that lead and trail the source on sky, as they should reveal systematics produced by nearby stars. The leading and trailing pixels are defined as those diagonal to the center from the bottom left to the upper right (the direction of motion of 3I/ATLAS). The light curve extracted from each pixel is binned at a 36 minute resolution. A Lomb-Scargle periodogram is performed on each resulting light curve across the same frequency range (Figure 8). There are some similarities between the leading/trailing pixels that do *not* align with the periodic signals observed from 3I/ATLAS. In particular, the trailing/leading pixels display a similar periodic signal at 29 hours in the data from Camera 2 CCD 3. This signal is offset from a peak in the 3I/ATLAS observations by ~ 4 hours. There are similar offsets between the trailing/leading and 3I/ATLAS pixels for Camera 1 CCD 2.

Given the similarities in noise properties of the periodograms, it is challenging to draw any confident conclusions about 3I/ATLAS. Therefore, we conclude that these *TESS* light curves do no definitively capture a P_{rot} from the nucleus. This may be due to ongoing outgassing even at large heliocentric distances or due to the sensitivity of *TESS*, making any possible magnitude changes from the baseline difficult to definitively measure.

3.3. Secular Light Curve

We calculated the inferred absolute V magnitude of 3I/ATLAS from these observations to add to the light curve presented in D. Z. Seligman et al. (2025). The secular light curve of a comet provides insight into the type of volatile driving activity — or at least the volatility of the species driving activity. For example, M. Womack et al. (2021) presented a 4 year secular light curve of C/1995 O1 (Hale-Bopp) to infer that CO was responsible for the activity exterior to 2.6–3.0 au, while H₂O was responsible for it interior to that.

We convert the calculated *TESS* magnitude to absolute V magnitude, H_V , using the following. T. L. Farnham et al. (2021) derived a rough relationship between the apparent visual magnitude, V , and *TESS* magnitude of

$$V = T_{\text{mag}} + 0.8. \quad (2)$$

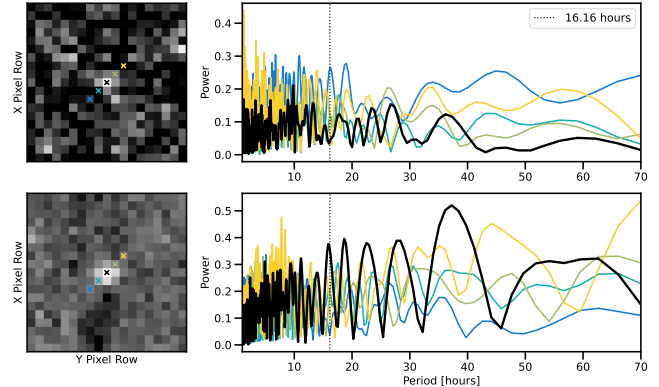


Figure 8. Comparison of the Lomb-Scargle periodogram for 3I/ATLAS (black) and trailing/leading pixels (colored). The pixels and corresponding periodograms are marked in the same color. The top/bottom row is for the observations from Camera 2 CCD 3/Camera 1 CCD 2. There is a strong periodic signal at 33 hours in the trailing and leading pixels, offset from the peak from 3I/ATLAS by ~ 4 hours. Moreover, these pixels all display some periodicity at $P = 20 - 30$ hours, comparable to that seen in 3I/ATLAS. There are similarities in the periodograms between 3I/ATLAS and the trailing/leading pixels such as the signals at 24 – 27 hours and at 35 – 41 hours. These similarities indicate that significant rotational information regarding 3I/ATLAS cannot be extracted from the *TESS* light curves. \bullet

This relationship was derived using the Web *TESS* Viewing Tool assuming typical comet colors derived from the average of several Jupiter Family comets, long-period comets, and active centaurs. This relationship has an uncertainty of ± 0.3 mag, which is dominated by the uncertainty in comet colors. We convert V to H_V using the following:

$$H_V = V - 2.5 n \log_{10}(d_{\odot}) - 5 \log_{10}(d_{\text{TESS}}). \quad (3)$$

In Equation 3, d_{\odot} is the comet-Sun distance, d_{TESS} is the comet-*TESS* distance, and n is an activity index. n has a typical range from $n = 2 - 6$, where $n = 2$ assumes the body is inactive and $n = 6$ assumes the object has strong activity (E. Everhart 1967). Given that 3I/ATLAS is at a distance of 6.4 au in these images, we assume $n = 2$.

We use the average d_{\odot} and d_{\oplus} for each Camera/CCD configuration presented in Table 1. From our calculated *TESS* magnitude, following Equations 2 and 3, and adopting the uncertainty presented in T. L. Farnham et al. (2021), we derive $H_V = 13.72 \pm 0.35$ and 12.52 ± 0.35 . We plot discovery and precovery ZTF observations of 3I/ATLAS in Figure 9.

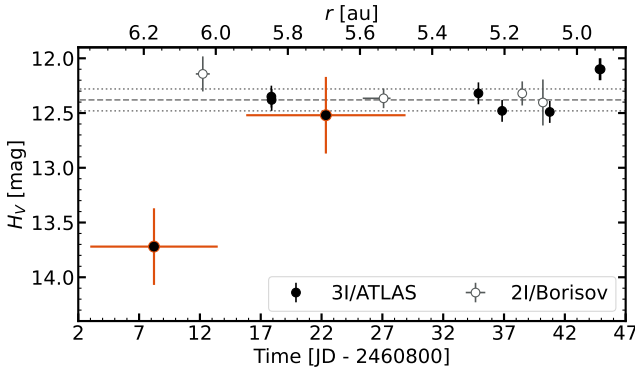


Figure 9. Absolute visual magnitude, H_V computed from *TESS* (orange) and ZTF observations of 3I/ATLAS (black) as compared to 2I/Borisov (gray). The median and 1σ standard deviations of the ZTF observations are plotted as dashed and dotted lines, respectively. The top axes represents the heliocentric distance of 3I/ATLAS and 2I/Borisov at the time of the observation. ZTF observations of 3I/ATLAS were derived in D. Z. Seligman et al. (2025); pre-perihelion observations of 2I/Borisov were derived in Q. Ye et al. (2020). We note that the lower time x-axis is applicable to 3I/ATLAS and not to 2I/Borisov. \bullet

502

4. DISCUSSION

We present two deepstack images and a 20-day light curve of 3I/ATLAS as observed with NASA’s *Transiting Exoplanet Survey Satellite*. These data were obtained from 07 May to 03 June 2025, predating the initial discovery by nearly two months (L. Denneau et al. 2025). From our two epochs of these data we calculate that 3I/ATLAS had a $T_{\text{mag}} = 20.83 \pm 0.05$ and $T_{\text{mag}} = 19.28 \pm 0.05$, the latter of which is consistent with more recently obtained R_C observations from the TRAPPIST-North and TRAPPIST-South telescopes (D. Z. Seligman et al. 2025). Moreover, we identify a periodic signal at ~ 16 hours in the light curve from Camera 1 CCD 2. However, we find no statistically significant evidence of a rotation period from the nucleus when comparing the light curve of 3I/ATLAS to a neighboring background pixel. The lack of observed rotation may be due to the presence of a coma, uncertainties in the size of the nucleus if there is no coma, or decreased sensitivity of *TESS* to faint objects.

The derived H_V from these data indicate that 3I/ATLAS brightened more than can be expected from the decrease in helio- and *TESS*-centric distances between the two periods. It is worth stating that the object traversed nearly 1 au during the course of these observations. We note that the absolute magnitude of 3I/ATLAS in our first epoch, $H_V=13.9$, is consistent with activity from

a small ($R < 2.8$ km, $H_V > 15.4$) nucleus derived from HST WFC3 imaging (D. Jewitt et al. 2025). This provides tentative evidence that 3I/ATLAS was active during the fortuitous TESS observations prior to its discovery on UT 01 July 2025. However, the 3σ error technically permits the possibility that 3I/ATLAS was fainter by ~ 1 magnitude during these observations. This is due to the uncertainties in the conversion from T_{mag} magnitudes to V of 0.3 (R. Vanderspek et al. 2018; T. L. Farnham et al. 2021). Therefore, we conclude that these observations are consistent with the hypothesis that 3I/ATLAS was weakly active prior to its discovery. Future work could include deriving a new relationship between T_{mag} and other bandpasses for ISOs.

This distant activity of 3I/ATLAS — if confirmed — could be indicative of mass loss driven by a mechanism other than the sublimation of H_2O ice. One possibility is that 3I/ATLAS is enriched in hypervolatiles such as CO or CO_2 . 2I/Borisov displayed a higher production of CO than H_2O when these two quantities were measured contemporaneously (D. Bodewits et al. 2020; M. A. Cordiner et al. 2020; Z. Xing et al. 2020), although no direct measurement of CO_2 has been successfully obtained in an interstellar object to date.⁵ It is also possible that this activity is driven by a more exotic hypervolatile such as H_2 or N_2 . The nongravitational acceleration of 1I/‘Oumuamua energetically would have required the sublimation of an ice more volatile than H_2O (Z. Sekanina 2019; D. Seligman & G. Laughlin 2020). It has therefore been proposed that this acceleration was driven by outgassing of N_2 (A. P. Jackson & S. J. Desch 2021), CO (D. Z. Seligman et al. 2021), or radiolytically produced H_2 (J. B. Bergner & D. Z. Seligman 2023). It is possible that distant activity of 3I/ATLAS is driven by one of these, but determining which neutral is responsible requires spectroscopic confirmation or long-term lightcurve modeling (E. Bufanda et al. 2023).

The change in absolute magnitude between our two deep stacks indicates a change in activity, likely the result of a rapidly warming thermal environment. Continued searches for precovery images and extensive monitoring of 3I/ATLAS prior to perihelion will be essential for characterizing this trend. In particular, other precovery images which may include stellar occultations of appulses (J. L. Ortiz et al. 2023; C. L. Pereira et al. 2025), especially from multi-filter observations, could constrain the coma density and composition. More

⁵ Production rates of CO_2 have been inferred from the ration of O I emission features in the visible, A. McKay et al. 2024

579 over, spectroscopic follow-up observations could also
 580 confirm the existence of hypervolatiles in 3I/ATLAS.

581 Observations of future ISOs could also shed light on
 582 the extent to which this population displays distant
 583 activity and is enriched with hypervolatiles. Existing
 584 all-sky surveys, including the new Rubin Observatory
 585 Legacy Survey of Space and Time (LSST) have been
 586 predicted to detect future ISOs (A. Moro-Martín et al.
 587 2009; T. Engelhardt et al. 2017; N. V. Cook et al. 2016;
 588 D. Seligman & G. Laughlin 2018; D. J. Hoover et al.
 589 2022; D. Miller et al. 2022; D. Landau et al. 2023; D.
 590 Marčeta 2023; D. Marčeta & D. Z. Seligman 2023; R. C.
 591 Dorsey et al. 2025). Reorienting *TESS* to observe the
 592 ecliptic for longer periods of time in future extended mis-
 593 sions could aid in the precovery observations of newly
 594 detected ISOs.

595 5. DATA AND SOFTWARE AVAILABILITY

596 The calibrated *TESS* FFIs are available for bulk
 597 download on the Mikulski Archive for Space Telescopes.⁶
 598 All of the analysis Python scripts, data behind the fig-
 599 ures, and Python scripts for reproducing the figures
 600 presented here are available on GitHub.⁷ Additional,
 601 larger, data products will be made available on Zenodo
 602 upon publication.

603 This work made use of the following open-source
 604 Python packages: `astropy` ([Astropy Collaboration](#)

605 et al. 2013, 2018, 2022), `numpy` (S. Van Der Walt et al.
 606 2011), `scipy` (P. Virtanen et al. 2020), `matplotlib`
 607 (J. D. Hunter et al. 2007).

608 6. ACKNOWLEDGMENTS

609 We thank Henry Hsieh, Davide Farnocchia, and Marco
 610 Micheli for thoughtful insights. **We thank the anonymous**
 611 **referee for their comments which have improved the quality and clarity of this manuscript.**
 612 A.D.F. acknowledges funding from NASA through the
 613 NASA Hubble Fellowship grant HST-HF2-51530.001-A
 614 awarded by STScI. D.Z.S. is supported by an NSF As-
 615 tronomy and Astrophysics Postdoctoral Fellowship un-
 616 der award AST-2303553. This research award is par-
 617 tially funded by a generous gift of Charles Simonyi to
 618 the NSF Division of Astronomical Sciences. The award
 619 is made in recognition of significant contributions to Ru-
 620 bin Observatory’s Legacy Survey of Space and Time.

622 7. AUTHOR CONTRIBUTIONS

623 A.D.F. lead the *TESS* data reduction, the creation
 624 of the deepstack images, the light curve extraction,
 625 manuscript writing, and figure creation. J.W.N. con-
 626 tributed manuscript text and review. D.Z.S. contributed
 627 manuscript text and review.

628 APPENDIX

629 In this appendix we include additional detail on our analysis. In particular, we focus on the back-
 630 ground removal in Section A and a more in-depth discussion of our aperture selections in Section B.

631 A. BACKGROUND REMOVAL

633 In Figure 10 we present the models and residuals tested to remove the background properties in the
 634 *TESS* FFIs. These experiments demonstrated that the Savitsky-Golay filter (with a window length of
 635 307) presents the optimal fit to the observations *without* overfitting the faint signal of 3I/ATLAS for
 636 Camera 2 CCD 3. The larger window length is also able to recover the target but improperly fits the
 637 sharp decline of the orbital ramp. The 2nd-order polynomial does not fit the Camera 1 CCD 2 data
 638 well due to the strong systematics present in the observations. Similarly to Camera 2 CCD 3, the
 639 second image is best fit by the Savitsky-Golay filter with a window length of 307. Therefore, we select
 640 this background to subtract from the calibrated FFIs in the entirety of the analysis presented in this
 641 work.

642 B. APERTURE SELECTION

643 The *TESS* pixel response function (PRF) can change substantially over a given camera’s FOV.
 644 Additionally, the PRF is slightly chromatic and can vary with temperature. The *TESS* PRF model

⁶ https://archive.stsci.edu/tess/bulk_downloads/bulk_downloads_ffi_tp_lc_dv.html

⁷ <https://github.com/afeinstein20/atlas-tess>

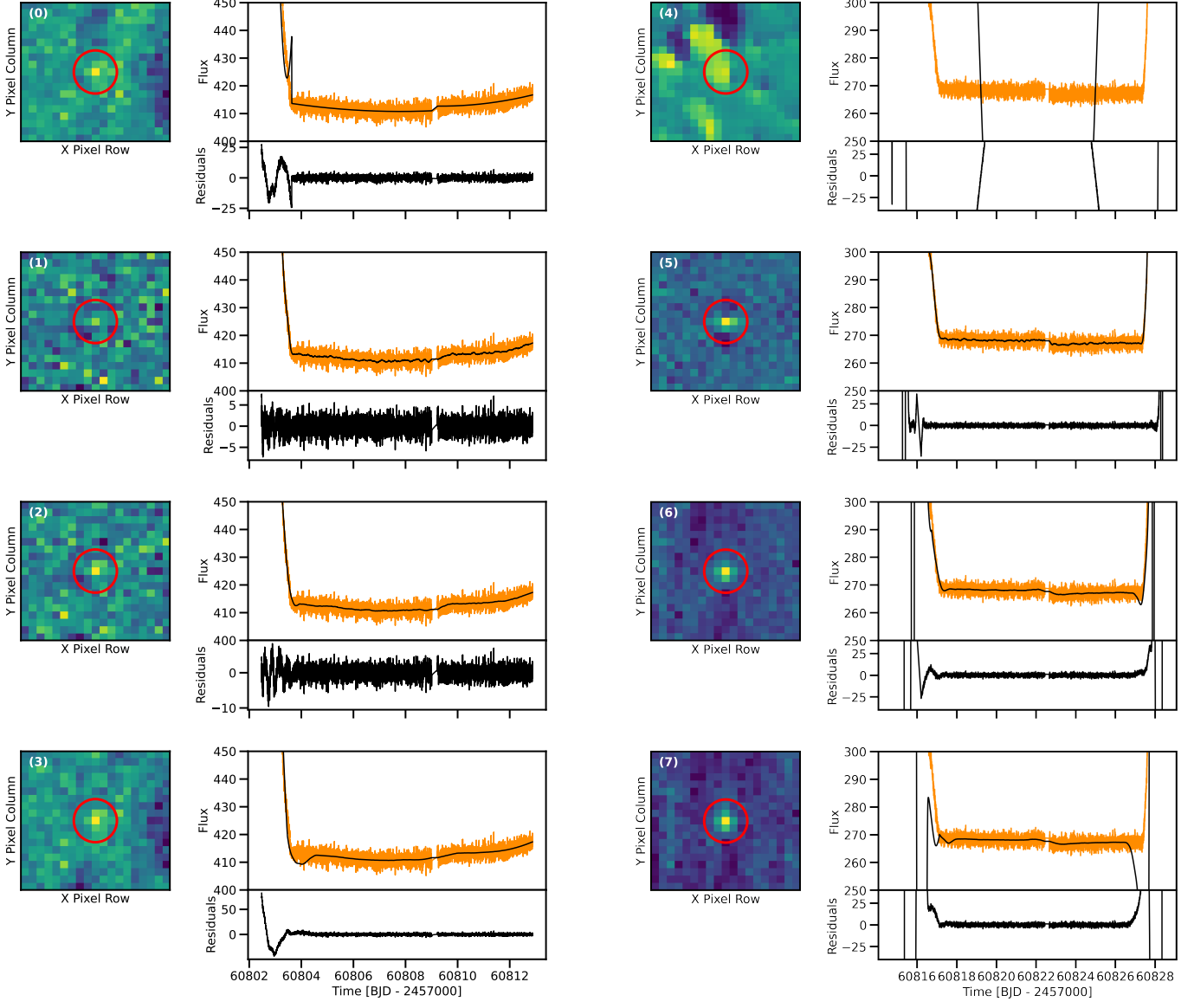


Figure 10. An example of the various background fits to each pixel. Subplots (0-3) are representative of Camera 2 CCD 3; subplots (4-7) are representative of Camera 1 CCD 2. The extracted calibrated flux is shown in orange, the best-fit model overplotted in black, and the resulting residuals underneath in black. The left panel of each subplot shows the median deepstack image after the shift-stack methodology is performed on and subtracted from each image. The first row presents a 2nd-order polynomial fit. The second, third, and fourth rows present a Savitsky-Golay filter model with window lengths of 121, 307, and 855, respectively.

assumes that 24% of the total source flux will be contained in the central pixel if the target is perfectly centered. If the target is offset, then the total amount of flux decreases. It is particularly important to take this into account when trying to extract the flux from a moving target. To combat these effects, larger apertures are more robust against these flux losses. However, implementing such large apertures is also particularly challenging for crowded fields because they may include flux contributions from nearby sources.

To investigate the efficacy of both competing effects, we perform a set of experiments on a variety of apertures to extract the light curve of 3I/ATLAS. The subset of apertures investigated here are provided in [A. D. Feinstein et al. \(2019\)](#), ranging from a single pixel to a 3×3 area. The results of these tests are presented in Figure 11 and Figure 12. These figures show the full light curve as well

as the light curve binned to 36 minutes. We also run the binned light curve through a Lomb-Scargle periodogram to search for potential evidence of a rotation period.

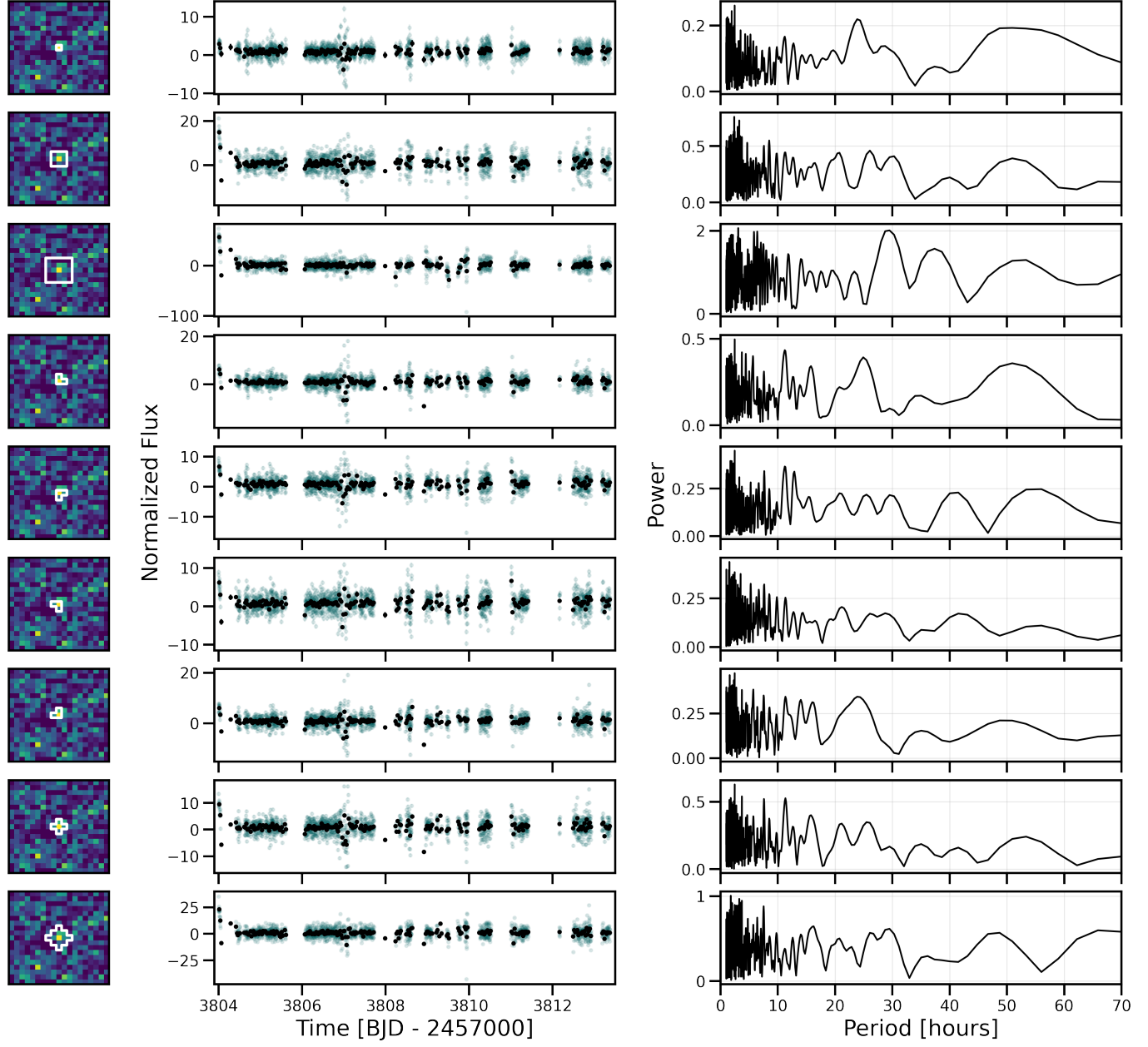


Figure 11. Testing different apertures to create the light curve of 3I/ATLAS from Camera 2 CCD 3. The first column is a contour overlay of the aperture we tested. We choose this selection of apertures based on those presented in [A. D. Feinstein et al. \(2019\)](#). Each aperture includes the central pixel and at least two surrounding pixels. The image colormap scaled to Figure 5. The middle column is the extracted normalized light curve. The unbinned light curve is plotted in blue while the data binned to 36 minutes is plotted in black. The right column is the periodogram of the binned data.

Figure 11 demonstrates that the light curve is dominated by noise at $P < 10$ hours. Additionally, there is no strong evidence of periodicity for $P > 30$ hours. While there are stronger peaks at $P = 15-28$ hours, the majority of these periodograms have peaks at identical times within this time range. We note that the periodograms shown in rows 5-8 of Figure 11 contain similar peaks at ~ 19 hours, which could be

consistent with the reported $P_{\text{rot}} = 16.79 \pm 0.23$ hours (R. de la Fuente Marcos et al. 2025). However, because the same signal is not seen across all extracted light curves, we attribute it to instrumental systematics.

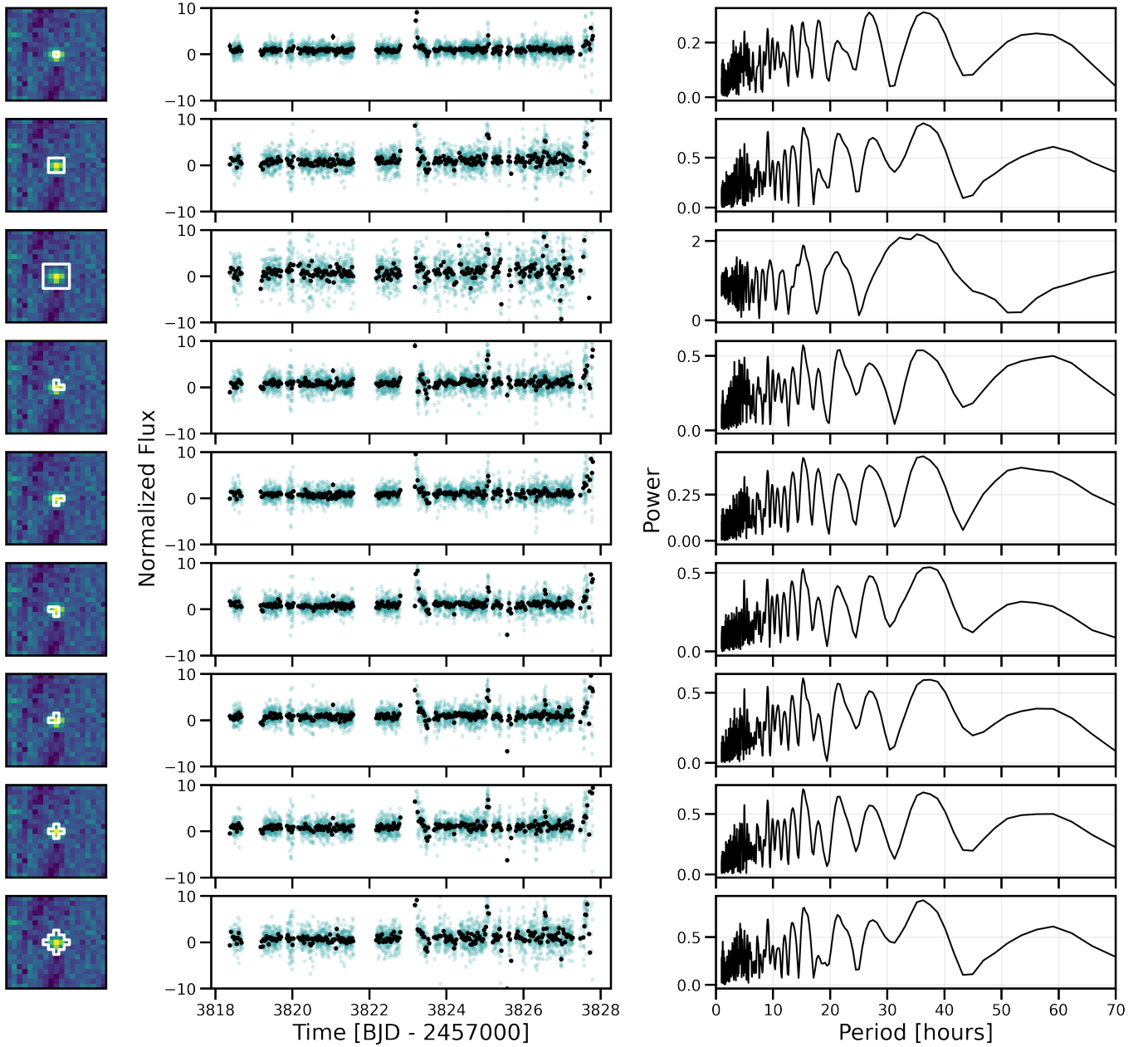


Figure 12. Same as Figure 11, but for our second epoch of observations from Camera 1 CCD 2.

We repeat this same test with the data extracted from Camera 1 CCD 2. These results are presented in Figure 12. Similarly to the previous analysis of the other *TESS* image, the $P < 10$ hours is dominated by noise. Contrary to the previous analysis however, there is a strong peak between 37 – 41 hours. Additionally, we find a consistent strong double-peaked feature at $P = 16, 22, 28$ hours. The 16 hour peak is consistent with P_{rot} recovered by (R. de la Fuente Marcos et al. 2025; T. Santana-Ros et al. 2025). These signals are strong in every extracted light curve. None of the stronger peaks seen in the light curves extracted from Camera 1 CCD 2 are consistent with those from Camera 2 CCD 3.

671 Additionally, because there are multiple strong peaks and no observable photometric variability in all
 672 data, it is challenging to determine whether the signals are instrumental or astrophysical in origin.
 673 Nevertheless, because the periodograms between *TESS* data sets are inconsistent, we conclude that
 674 we are unable to measure a rotation period from these observations.

REFERENCES

- 675 Alarcon, M. R., Serra-Ricart, M., Licandro, J., et al. 2025,
 676 Deep g¹-band Imaging of Interstellar Comet 3I/ATLAS
 677 from the Two-meter Twin Telescope (TTT),, The
 678 Astronomer's Telegram, No. 17264
<https://www.astronomerstelegram.org/?read=17264>
- 680 Andrews, J. E., Shrestha, M., Bostroem, K. A., et al. 2025,
 681 ApJ, 980, 37, doi: [10.3847/1538-4357/ada555](https://doi.org/10.3847/1538-4357/ada555)
- 682 Aravind, K., Ganesh, S., Venkataramani, K., et al. 2021,
 683 MNRAS, 502, 3491, doi: [10.1093/mnras/stab084](https://doi.org/10.1093/mnras/stab084)
- 684 Astropy Collaboration, Robitaille, T. P., Tollerud, E. J.,
 685 et al. 2013, A&A, 558, A33,
 686 doi: [10.1051/0004-6361/201322068](https://doi.org/10.1051/0004-6361/201322068)
- 687 Astropy Collaboration, Price-Whelan, A. M., Sipőcz, B. M.,
 688 et al. 2018, AJ, 156, 123, doi: [10.3847/1538-3881/aabc4f](https://doi.org/10.3847/1538-3881/aabc4f)
- 689 Astropy Collaboration, Price-Whelan, A. M., Lim, P. L.,
 690 et al. 2022, ApJ, 935, 167, doi: [10.3847/1538-4357/ac7c74](https://doi.org/10.3847/1538-4357/ac7c74)
- 691 Bagnulo, S., Cellino, A., Kolokolova, L., et al. 2021, Nature
 692 Communications, 12, 1797,
 693 doi: [10.1038/s41467-021-22000-x](https://doi.org/10.1038/s41467-021-22000-x)
- 694 Bannister, M. T., Schwamb, M. E., Fraser, W. C., et al.
 695 2017, ApJL, 851, L38, doi: [10.3847/2041-8213/aaa07c](https://doi.org/10.3847/2041-8213/aaa07c)
- 696 Bannister, M. T., Opitom, C., Fitzsimmons, A., et al. 2020,
 697 arXiv e-prints, arXiv:2001.11605.
<https://arxiv.org/abs/2001.11605>
- 698 Belton, M. J. S., Hainaut, O. R., Meech, K. J., et al. 2018,
 699 ApJL, 856, L21, doi: [10.3847/2041-8213/aab370](https://doi.org/10.3847/2041-8213/aab370)
- 700 Bergner, J. B., & Seligman, D. Z. 2023, Nature, 615, 610,
 701 doi: [10.1038/s41586-022-05687-w](https://doi.org/10.1038/s41586-022-05687-w)
- 702 Bodewits, D., Noonan, J. W., Feldman, P. D., et al. 2020,
 703 Nature Astronomy, 4, 867,
 704 doi: [10.1038/s41550-020-1095-2](https://doi.org/10.1038/s41550-020-1095-2)
- 705 Borisov, G., Durig, D. T., Sato, H., et al. 2019, Central
 706 Bureau Electronic Telegrams, 4666, 1
- 707 Bufanda, E., Meech, K., Kleyna, J., Keane, J., & Hainaut,
 708 O. 2023, in AAS/Division for Planetary Sciences Meeting
 709 Abstracts, Vol. 55, AAS/Division for Planetary Sciences
 710 Meeting Abstracts #55, 400.09
- 711 Burke, C. J., Levine, A., Fausnaugh, M., et al. 2020,
 712 TESS-Point: High precision TESS pointing tool,,
 713 Astrophysics Source Code Library, record ascl:2003.001
- 714 Chandler, C. O., Bernardinelli, P. H., Jurić, M., et al. 2025,
 715 arXiv e-prints, arXiv:2507.13409,
 716 doi: [10.48550/arXiv.2507.13409](https://doi.org/10.48550/arXiv.2507.13409)
- 717 Cook, N. V., Ragozzine, D., Granvik, M., & Stephens, D. C.
 718 2016, ApJ, 825, 51, doi: [10.3847/0004-637X/825/1/51](https://doi.org/10.3847/0004-637X/825/1/51)
- 719 Cordiner, M. A., Milam, S. N., Biver, N., et al. 2020, Nature
 720 Astronomy, 4, 861, doi: [10.1038/s41550-020-1087-2](https://doi.org/10.1038/s41550-020-1087-2)
- 721 Cremonese, G., Fulle, M., Cambianica, P., et al. 2020,
 722 ApJL, 893, L12, doi: [10.3847/2041-8213/ab8455](https://doi.org/10.3847/2041-8213/ab8455)
- 723 de la Fuente Marcos, R., Licandro, J., Alarcon, M. R., et al.
 724 2025, arXiv e-prints, arXiv:2507.12922.
<https://arxiv.org/abs/2507.12922>
- 725 Deam, S. E., Bannister, M. T., Opitom, C., et al. 2025,
 726 arXiv e-prints, arXiv:2507.05051,
 727 doi: [10.48550/arXiv.2507.05051](https://doi.org/10.48550/arXiv.2507.05051)
- 728 Denneau, L., Siverd, R., Tonry, J., et al. 2025, MPEC
- 729 Dorsey, R. C., Hopkins, M. J., Bannister, M. T., et al.
 730 2025, arXiv e-prints, arXiv:2502.16741,
 731 doi: [10.48550/arXiv.2502.16741](https://doi.org/10.48550/arXiv.2502.16741)
- 732 Drahus, M., Yang, B., Lis, D. C., & Jewitt, D. 2017,
 733 MNRAS, 468, 2897, doi: [10.1093/mnras/stw2227](https://doi.org/10.1093/mnras/stw2227)
- 734 Engelhardt, T., Jedicke, R., Vereš, P., et al. 2017,
 735 Astronomical Journal, 153, 133,
 736 doi: [10.3847/1538-3881/aa5c8a](https://doi.org/10.3847/1538-3881/aa5c8a)
- 737 Everhart, E. 1967, AJ, 72, 716, doi: [10.1086/110299](https://doi.org/10.1086/110299)
- 738 Farnham, T. L., Kelley, M. S. P., & Bauer, J. M. 2021,
 739 PSJ, 2, 236, doi: [10.3847/PSJ/ac323d](https://doi.org/10.3847/PSJ/ac323d)
- 740 Farnham, T. L., Kelley, M. S. P., Knight, M. M., & Feaga,
 741 L. M. 2019, ApJL, 886, L24,
 742 doi: [10.3847/2041-8213/ab564d](https://doi.org/10.3847/2041-8213/ab564d)
- 743 Fausnaugh, M. M., Valley, P. J., Tucker, M. A., et al. 2023,
 744 ApJ, 956, 108, doi: [10.3847/1538-4357/aceaf](https://doi.org/10.3847/1538-4357/aceaf)
- 745 Feinstein, A. D., Montet, B. T., Foreman-Mackey, D., et al.
 746 2019, PASP, 131, 094502, doi: [10.1088/1538-3873/ab291c](https://doi.org/10.1088/1538-3873/ab291c)
- 747 Fitzsimmons, A., Meech, K., Matrà, L., & Pfalzner, S.
 748 2024, in Comets III, ed. K. J. Meech, M. R. Combi,
 749 D. Bockelée-Morvan, S. N. Raymond, & M. E. Zolensky,
 750 731–766
- 751 Fitzsimmons, A., Snodgrass, C., Rozitis, B., et al. 2018,
 752 Nature Astronomy, 2, 133,
 753 doi: [10.1038/s41550-017-0361-4](https://doi.org/10.1038/s41550-017-0361-4)
- 754 Fitzsimmons, A., Hainaut, O., Meech, K. J., et al. 2019,
 755 ApJL, 885, L9, doi: [10.3847/2041-8213/ab49fc](https://doi.org/10.3847/2041-8213/ab49fc)
- 756 Fraser, W. C., Pravec, P., Fitzsimmons, A., et al. 2018,
 757 Nature Astronomy, 2, 383,
 758 doi: [10.1038/s41550-018-0398-z](https://doi.org/10.1038/s41550-018-0398-z)

- 761 Fraser, W. C., Porter, S. B., Peltier, L., et al. 2024, PSJ, 5, 5
 762 227, doi: [10.3847/PSJ/ad6f9e](https://doi.org/10.3847/PSJ/ad6f9e)
- 763 Gaidos, E., Williams, J., & Kraus, A. 2017, RNAAS, 1, 13,
 764 doi: [10.3847/2515-5172/aa9851](https://doi.org/10.3847/2515-5172/aa9851)
- 765 Guzik, P., Drahus, M., Rusek, K., et al. 2020, Nature
 766 Astronomy, 4, 53, doi: [10.1038/s41550-019-0931-8](https://doi.org/10.1038/s41550-019-0931-8)
- 767 Hoover, D. J., Seligman, D. Z., & Payne, M. J. 2022,
 768 Planetary Science Journal, 3, 71, doi: [10.3847/PSJ/ac58fe](https://doi.org/10.3847/PSJ/ac58fe)
- 769 Hui, M.-T., & Knight, M. M. 2019, AJ, 158, 256,
 770 doi: [10.3847/1538-3881/ab50b8](https://doi.org/10.3847/1538-3881/ab50b8)
- 771 Hui, M.-T., Ye, Q.-Z., Föhring, D., Hung, D., & Tholen,
 772 D. J. 2020, AJ, 160, 92, doi: [10.3847/1538-3881/ab9df8](https://doi.org/10.3847/1538-3881/ab9df8)
- 773 Hunter, J. D., et al. 2007, Computing in science and
 774 engineering, 9, 90
- 775 Jackson, A. P., & Desch, S. J. 2021, Journal of Geophysical
 776 Research (Planets), 126, e06706,
 777 doi: [10.1029/2020JE006706](https://doi.org/10.1029/2020JE006706)
- 778 Jewitt, D., Hui, M.-T., Mutchler, M., Kim, Y., & Agarwal,
 779 J. 2025, Hubble Space Telescope Observations of the
 780 Interstellar Interloper 3I/ATLAS,
 781 <https://arxiv.org/abs/2508.02934>
- 782 Jewitt, D., & Luu, J. 2019, ApJL, 886, L29,
 783 doi: [10.3847/2041-8213/ab530b](https://doi.org/10.3847/2041-8213/ab530b)
- 784 Jewitt, D., & Luu, J. 2025, Interstellar Interloper C/2025
 785 N1 is Active,, The Astronomer's Telegram, No. 17263
 786 <https://www.astronomerstelegram.org/?read=17263>
- 787 Jewitt, D., Luu, J., Rajagopal, J., et al. 2017, Astrophysical
 788 Journal Letters, 850, L36, doi: [10.3847/2041-8213/aa9b2f](https://doi.org/10.3847/2041-8213/aa9b2f)
- 789 Jewitt, D., & Seligman, D. Z. 2023, ARA&A, 61, 197,
 790 doi: [10.1146/annurev-astro-071221-054221](https://doi.org/10.1146/annurev-astro-071221-054221)
- 791 Karetta, T., Andrews, J., Noonan, J. W., et al. 2020, ApJL,
 792 889, L38, doi: [10.3847/2041-8213/ab6a08](https://doi.org/10.3847/2041-8213/ab6a08)
- 793 Karetta, T., Champagne, C., McClure, L., et al. 2025, arXiv
 794 e-prints, arXiv:2507.12234.
 795 <https://arxiv.org/abs/2507.12234>
- 796 Kim, Y., Jewitt, D., Mutchler, M., et al. 2020, ApJL, 895,
 797 L34, doi: [10.3847/2041-8213/ab9228](https://doi.org/10.3847/2041-8213/ab9228)
- 798 Kiss, C., Takács, N., Kalup, C. E., et al. 2025, A&A, 694,
 799 L17, doi: [10.1051/0004-6361/202453509](https://doi.org/10.1051/0004-6361/202453509)
- 800 Knight, M. M., Protopapa, S., Kelley, M. S. P., et al. 2017,
 801 Astrophysical Journal Letters, 851, L31,
 802 doi: [10.3847/2041-8213/aa9d81](https://doi.org/10.3847/2041-8213/aa9d81)
- 803 Landau, D., Donitz, B., & Karimi, R. 2023, Acta
 804 Astronautica, 206, 133,
 805 doi: [10.1016/j.actaastro.2023.02.021](https://doi.org/10.1016/j.actaastro.2023.02.021)
- 806 Lin, H. W., Lee, C.-H., Gerdes, D. W., et al. 2020, ApJL,
 807 889, L30, doi: [10.3847/2041-8213/ab6bd9](https://doi.org/10.3847/2041-8213/ab6bd9)
- 808 Lomb, N. R. 1976, Ap&SS, 39, 447,
 809 doi: [10.1007/BF00648343](https://doi.org/10.1007/BF00648343)
- 810 Mamajek, E. 2017, Research Notes of the American
 811 Astronomical Society, 1, 21,
 812 doi: [10.3847/2515-5172/aa9bdc](https://doi.org/10.3847/2515-5172/aa9bdc)
- 813 Martinez-Palomera, J., Tucson, A., Hedges, C., et al. 2025,
 814 arXiv e-prints, arXiv:2508.02499,
 815 doi: [10.48550/arXiv.2508.02499](https://doi.org/10.48550/arXiv.2508.02499)
- 816 Marčeta, D. 2023, Astronomy and Computing, 42, 100690,
 817 doi: [10.1016/j.ascom.2023.100690](https://doi.org/10.1016/j.ascom.2023.100690)
- 818 Marčeta, D., & Seligman, D. Z. 2023, Planetary Science
 819 Journal, 4, 230, doi: [10.3847/PSJ/ad08c1](https://doi.org/10.3847/PSJ/ad08c1)
- 820 Mashchenko, S. 2019, MNRAS, 489, 3003,
 821 doi: [10.1093/mnras/stz2380](https://doi.org/10.1093/mnras/stz2380)
- 822 Masiero, J. 2017, arXiv e-prints, arXiv:1710.09977.
 823 <https://arxiv.org/abs/1710.09977>
- 824 Masiero, J. R., Grav, T., Mainzer, A. K., et al. 2014, ApJ,
 825 791, 121, doi: [10.1088/0004-637X/791/2/121](https://doi.org/10.1088/0004-637X/791/2/121)
- 826 McKay, A., Opitom, C., Jehin, E., et al. 2024, in
 827 AAS/Division for Planetary Sciences Meeting Abstracts,
 828 Vol. 56, 56th Annual Meeting of the Division for
 829 Planetary Sciences, 301.01
- 830 McKay, A. J., Cochran, A. L., Dello Russo, N., & DiSanti,
 831 M. A. 2020, ApJL, 889, L10,
 832 doi: [10.3847/2041-8213/ab64ed](https://doi.org/10.3847/2041-8213/ab64ed)
- 833 Meech, K. J., Weryk, R., Micheli, M., et al. 2017, Nature,
 834 552, 378, doi: [10.1038/nature25020](https://doi.org/10.1038/nature25020)
- 835 Micheli, M., Farnocchia, D., Meech, K. J., et al. 2018,
 836 Nature, 559, 223, doi: [10.1038/s41586-018-0254-4](https://doi.org/10.1038/s41586-018-0254-4)
- 837 Miller, D., Duvigneaud, F., Menken, W., Landau, D., &
 838 Linares, R. 2022, Acta Astronautica, 200, 242,
 839 doi: [10.1016/j.actaastro.2022.07.053](https://doi.org/10.1016/j.actaastro.2022.07.053)
- 840 Moro-Martín, A. 2022, arXiv e-prints, arXiv:2205.04277,
 841 doi: [10.48550/arXiv.2205.04277](https://doi.org/10.48550/arXiv.2205.04277)
- 842 Moro-Martín, A., Turner, E. L., & Loeb, A. 2009,
 843 Astrophysical Journal, 704, 733,
 844 doi: [10.1088/0004-637X/704/1/733](https://doi.org/10.1088/0004-637X/704/1/733)
- 845 Opitom, C., Fitzsimmons, A., Jehin, E., et al. 2019, A&A,
 846 631, L8, doi: [10.1051/0004-6361/201936959](https://doi.org/10.1051/0004-6361/201936959)
- 847 Opitom, C., Snodgrass, C., Jehin, E., et al. 2025, Initial
 848 VLT/MUSE spectroscopy of the interstellar object
 849 3I/ATLAS, <https://arxiv.org/abs/2507.05226>
- 850 Ortiz, J. L., Pereira, C. L., Sicardy, B., et al. 2023, A&A,
 851 676, L12, doi: [10.1051/0004-6361/202347025](https://doi.org/10.1051/0004-6361/202347025)
- 852 Pál, A., Szakáts, R., Kiss, C., et al. 2020, ApJS, 247, 26,
 853 doi: [10.3847/1538-4365/ab64f0](https://doi.org/10.3847/1538-4365/ab64f0)
- 854 Pereira, C. L., Braga-Ribas, F., Sicardy, B., et al. 2025,
 855 Philosophical Transactions of the Royal Society of
 856 London Series A, 383, 20240189,
 857 doi: [10.1098/rsta.2024.0189](https://doi.org/10.1098/rsta.2024.0189)
- 858 Polakis, T. 2018, Minor Planet Bulletin, 45, 347

- 859 Ricker, G. R., Winn, J. N., Vanderspek, R., et al. 2015,
 860 *Journal of Astronomical Telescopes, Instruments, and*
 861 *Systems*, 1, 014003, doi: [10.1111/JATIS.1.1.014003](https://doi.org/10.1111/JATIS.1.1.014003)
- 862 Santana-Ros, T., Ivanova, O., Mykhailova, S., et al. 2025,
 863 arXiv e-prints, arXiv:2508.00808,
 864 doi: [10.48550/arXiv.2508.00808](https://doi.org/10.48550/arXiv.2508.00808)
- 865 Scargle, J. D. 1982, *ApJ*, 263, 835, doi: [10.1086/160554](https://doi.org/10.1086/160554)
- 866 Sekanina, Z. 2019, arXiv e-prints, arXiv:1905.00935,
 867 doi: [10.48550/arXiv.1905.00935](https://doi.org/10.48550/arXiv.1905.00935)
- 868 Seligman, D., & Laughlin, G. 2018, *AJ*, 155, 217,
 869 doi: [10.3847/1538-3881/aabd37](https://doi.org/10.3847/1538-3881/aabd37)
- 870 Seligman, D., & Laughlin, G. 2020, *ApJL*, 896, L8,
 871 doi: [10.3847/2041-8213/ab963f](https://doi.org/10.3847/2041-8213/ab963f)
- 872 Seligman, D. Z., Levine, W. G., Cabot, S. H. C., Laughlin,
 873 G., & Meech, K. 2021, *ApJ*, 920, 28,
 874 doi: [10.3847/1538-4357/ac1594](https://doi.org/10.3847/1538-4357/ac1594)
- 875 Seligman, D. Z., & Moro-Martín, A. 2023, *Contemporary*
 876 *Physics*, 63, 200, doi: [10.1080/00107514.2023.2203976](https://doi.org/10.1080/00107514.2023.2203976)
- 877 Seligman, D. Z., Micheli, M., Farnocchia, D., et al. 2025,
 878 arXiv e-prints, arXiv:2507.02757,
 879 doi: [10.48550/arXiv.2507.02757](https://doi.org/10.48550/arXiv.2507.02757)
- 880 Szabó, G. M., Pál, A., Szigeti, L., et al. 2022, *A&A*, 661,
 881 A48, doi: [10.1051/0004-6361/202142223](https://doi.org/10.1051/0004-6361/202142223)
- 882 Taylor, A. G., Seligman, D. Z., Hainaut, O. R., & Meech,
 883 K. J. 2023, *PSJ*, 4, 186, doi: [10.3847/PSJ/acf617](https://doi.org/10.3847/PSJ/acf617)
- 884 Tonry, J. L., Denneau, L., Heinze, A. N., et al. 2018a,
 885 *PASP*, 130, 064505, doi: [10.1088/1538-3873/aabadf](https://doi.org/10.1088/1538-3873/aabadf)
- 886 Tonry, J. L., Denneau, L., Flewelling, H., et al. 2018b, *ApJ*,
 887 867, 105, doi: [10.3847/1538-4357/aae386](https://doi.org/10.3847/1538-4357/aae386)
- 888 Trilling, D. E., Mommert, M., Hora, J. L., et al. 2018,
 889 *Astronomical Journal*, 156, 261
- 890 Van Der Walt, S., Colbert, S. C., & Varoquaux, G. 2011,
 891 *Computing in Science & Engineering*, 13, 22
- 892 Vanderspek, R., Doty, J. P., Fausnaugh, M., et al. 2018,
 893 *TESS Instrument Handbook*, v0.1, Mikulski Archive for
 894 Space Telescopes, https://archive.stsci.edu/missions/tess/doc/TESS_Instrument_Handbook_v0.1.pdf
- 895 Virtanen, P., Gommers, R., Oliphant, T. E., et al. 2020,
 896 *Nature Methods*, 17, 261, doi: [10.1038/s41592-019-0686-2](https://doi.org/10.1038/s41592-019-0686-2)
- 897 Warner, B. D., Harris, A. W., & Pravec, P. 2009, *Icarus*,
 898 202, 134, doi: [10.1016/j.icarus.2009.02.003](https://doi.org/10.1016/j.icarus.2009.02.003)
- 900 Williams, G. V., Sato, H., Sarnecký, K., et al. 2017,
 901 *Central Bureau Electronic Telegrams*, 4450, 1
- 902 Womack, M., Curtis, O., Rabson, D. A., et al. 2021, *PSJ*, 2,
 903 17, doi: [10.3847/PSJ/abd32c](https://doi.org/10.3847/PSJ/abd32c)
- 904 Xing, Z., Bodewits, D., Noonan, J., & Bannister, M. T.
 905 2020, *ApJL*, 893, L48, doi: [10.3847/2041-8213/ab86be](https://doi.org/10.3847/2041-8213/ab86be)
- 906 Yang, B., Meech, K. J., Connelley, M., & Keane, J. V.
 907 2025, arXiv e-prints, arXiv:2507.14916.
 908 <https://arxiv.org/abs/2507.14916>
- 909 Yang, B., Li, A., Cordiner, M. A., et al. 2021, *Nature*
 910 *Astronomy*, doi: [10.1038/s41550-021-01336-w](https://doi.org/10.1038/s41550-021-01336-w)
- 911 Ye, Q., Kelley, M. S. P., Bolin, B. T., et al. 2020, *AJ*, 159,
 912 77, doi: [10.3847/1538-3881/ab659b](https://doi.org/10.3847/1538-3881/ab659b)
- 913 Ye, Q.-Z., Zhang, Q., Kelley, M. S. P., & Brown, P. G.
 914 2017, *Astrophysical Journal Letters*, 851, L5,
 915 doi: [10.3847/2041-8213/aa9a34](https://doi.org/10.3847/2041-8213/aa9a34)